The Astrophysical Journal, 907:69 (9pp), 2021 February 1 https://doi.org/10.3847/1538-4357/abc61c

New Ritz Wavelengths and Transition Probabilities of Parity-forbidden [Mn II] Lines of Astrophysical Interest

Florence S. Liggins[1], Juliet C. Pickering[1], Gillian Nave[2], Alexander Kramida[2], Sébastien Gamrath[3], and Pascal Quinet[3,4]

[1] Physics Dept., Imperial College London, Prince Consort Road, London SW7 2AZ, UK; j.pickering@imperial.ac.uk
[2] National Institute of Standards and Technology, Gaithersburg, MD 20899-8422, USA
[3] Physique Atomique et Astrophysique, Université de Mons–UMONS, 20 Place du Parc, B-7000 Mons, Belgium
[4] IPNAS, Université de Liège, B-4000 Liège, Belgium

Received 2020 March 20; revised 2020 October 6; accepted 2020 October 21; published 2021 January 29

Abstract

We report a comprehensive list of accurate Ritz wavelengths and calculated transition probabilities for parity-forbidden [Mn II] lines. Ritz wavelengths have been derived from experimentally established energy level values resulting from an extensive analysis of a high-resolution Fourier-transform emission spectrum of singly ionized manganese. Our analysis includes transitions between all known metastable and other long-lived levels of Mn II giving a total of 1130 [Mn II] Ritz wavelengths. Our entire list of derived Ritz wavelengths for [Mn II] lines ranges between 237 nm and 170 μm (42,125–58 cm^{-1}). The accurate Ritz wavelengths and calculated transition probabilities for forbidden lines in this paper are useful in the study and diagnostics of nebulae and other low-density astrophysical plasmas.

Unified Astronomy Thesaurus concepts: Atomic data benchmarking (2064); Atomic physics (2063); Line positions (2085); Spectral line lists (2082); Line intensities (2084); Laboratory astrophysics (2004); Theoretical techniques (2093); High resolution spectroscopy (2096); Atomic spectroscopy (2099)

Supporting material: machine-readable tables

1. Introduction

Nebular physics casts light on the structure, properties, and dynamics of diffuse astrophysical plasmas, through observations of vast clouds of ionized material, which may have been expelled during the death of a giant star, or be reassembling in preparation for the birth of another. Whereas the spectra of stellar atmospheres are rich in absorption lines, due to electric dipole (E1) transitions, nebular spectra exhibit strong emission lines, which arise as a result of various excitation mechanisms. Many of these emission lines are due to so-called "forbidden transitions" that originate from long-lived, low-lying metastable energy levels. E1 radiative transitions require a change in parity between upper and lower energy levels (see Table 1) and since the metastables and the ground level of an atom possess the same parity, radiative de-excitation through this mechanism is forbidden. Higher order, magnetic dipole (M1), and electric quadrupole (E2) radiative transitions are observed, but their transition probabilities are many orders of magnitude lower than for E1 transitions. Therefore in the spectra of stars and laboratory plasmas forbidden lines are rarely observed, as electrons occupying the metastable levels are likely to depopulate through collisional as opposed to radiative de-excitation. However, forbidden lines feature prevalently in the spectra of diffuse, low-density astrophysical plasmas, where collisions are rare and there is enough time for electrons to de-excite through M1 or E2 radiative transitions. They are thus frequently used as a diagnostic tool for these plasmas. The intensity ratios can provide an estimate of the density and temperature of the plasma, and lines are also used in determining the different chemical abundances. Both accurate wavelengths and knowledge of the transition probabilities of the forbidden lines are necessary parameters in these types of measurements, and although typically only pairs of transitions are used, this is partly due to the lack of available atomic data for these types of transitions.

In this paper we report a comprehensive list of Ritz wavelengths and calculated transition probabilities of forbidden lines in the spectrum of singly ionized manganese. Some of these [Mn II] lines have already been identified in the emission spectra of the peculiar super star η Carinae and its surrounding nebulosity by Wallerstein et al. (2001) and Hartman et al. (2004). We derived the Ritz wavelengths from optimized energy level values for the lowest-lying even-parity terms of Mn II. These levels were optimized through analysis of observed allowed Mn II transitions measured in hollow cathode lamps (HCL) using high-resolution Fourier-transform (FT) spectroscopy and are presented in a companion paper (Liggins et al. 2021). Although this analysis includes spectra from both FT and grating spectrometers, the grating spectra are of much lower resolution and thus have little influence on the positions of the metastable energy levels. Transition probabilities were calculated for all the lines from three different calculations, each of which used a semi-empirical pseudo-relativistic Hartree–Fock model. The uncertainties of the transition probabilities were estimated using Monte Carlo simulations.

2. Laboratory Data

Ritz wavelengths for the parity-forbidden [Mn II] lines were derived using the optimized energy level values resulting from an extensive analysis of the Mn II spectrum (Liggins 2017; Liggins et al. 2021). Accurate values of the metastable energy levels can be determined from allowed transitions involving these levels that give strong lines in FT spectra. The strongest lines were found in the ultraviolet (UV) spectral region, but lines used in this analysis were taken from all spectral regions from the infrared (IR) to the vacuum UV (VUV).

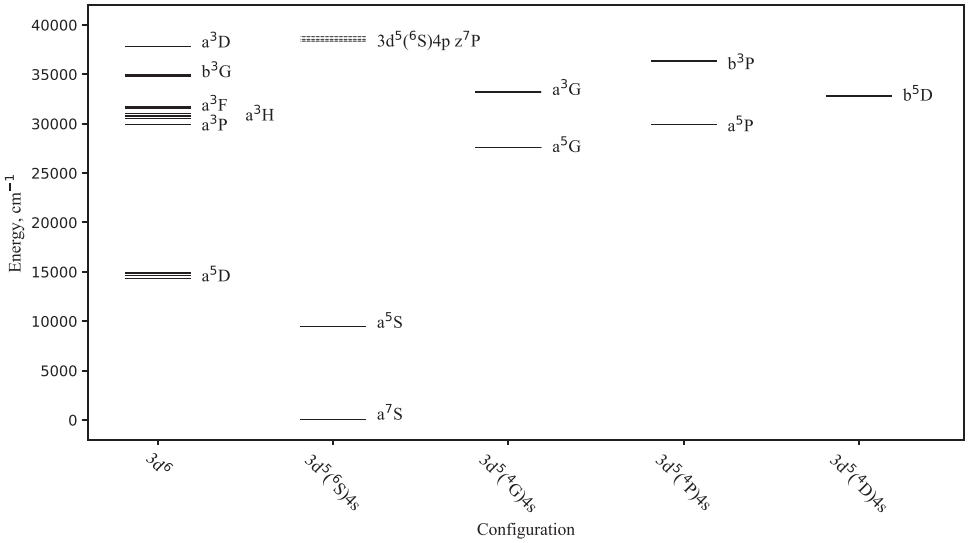

Figure 1. A partial energy level diagram showing the ground term, 3d^5(^{6}S)4 s a^{7}S, and the 40 even-parity metastable levels of Mn II. The dashed lines show the lowest-lying levels of odd parity, belonging to the 3d^5(^{6}S)4p z^{7}P term, for reference.

Table 1
Transition Rules for Allowed E1, and Parity-forbidden M1 and E2 Transitions

Trans.	Parity	ΔJ	Restrictions
E1	Change	0, ± 1	(0 ↮ 0)
M1	No Change	0, ± 1	(0 ↮ 0)
E2	No Change	0, ± 1, ± 2	(0 ↮ 0, $\frac{1}{2}$ ↮ $\frac{1}{2}$, 0 ↮ 1)

The Mn II spectrum was excited in water-cooled HCL run in either argon or neon. Spectra were measured at both Imperial College London (ICL) and the National Institute of Standards and Technology (NIST) using high-resolution FT spectrometry. The 2 m FT spectrometer at NIST, was used to measure the region 1820 cm^{-1} to 26,635 cm^{-1} (5494–375 nm). The region 24,005 cm^{-1} to 58,990 cm^{-1} (417–170 nm), was recorded at ICL using both the IC ultraviolet (UV) FT spectrometer (Thorne et al. 1987) and IC vacuum-ultraviolet (VUV) FT spectrometer (Thorne 1996). Some additional lines were taken from the high-current spectra of Kling & Griesmann (2000), which were recorded using the NIST FT700 spectrometer for the purpose of branching fraction measurements. Hollow cathodes used at ICL and NIST were composed of Mn:Ni and Mn:Cu alloy, respectively. A summary of all acquired spectra used in this analysis is given in Table 2.9 of Liggins (2017) and Table 1 of Liggins et al. (2021). Further details can be found in Kling & Griesmann (2000), Blackwell-Whitehead (2003), Liggins (2017), and Liggins et al. (2021).

The profiles of the spectral lines were fitted using the software XGREMLIN (Nave et al. 2015), from which accurate transition wavenumbers were obtained (Liggins et al. 2021). Since manganese has an odd number of nucleons, many spectral lines of Mn II exhibit hyperfine structure (HFS) and cannot be fitted with a simple Voigt profile. For most lines, a center-of-gravity fit was taken, giving the centroid wavenumber of the line profile. For some key lines exhibiting large hyperfine splitting, the wavenumber was taken from a fit to the HFS. The observed lines were wavelength-calibrated using Ar II standard lines taken from Whaling et al. (1995). The total wavenumber uncertainty for a given observed line was taken to be the quadrature sum of the uncertainty due to the line fitting and the uncertainty due to the calibration correction. Further details of the uncertainty analysis are given in Liggins (2017) and Liggins et al. (2021). For the majority of lines the resulting line wavenumbers and wavelengths are up to an order of magnitude more accurate than those of the previous large-scale work on Mn II given in Kramida & Sansonetti (2013, hereafter KS), this is due to the high accuracy of high-resolution FT spectra from IR to VUV spectral range used in the newer work.

3. Analysis

The energy level structure of Mn II is complex, with the lowest levels comprising 40 metastables, in addition to the ground state, 3d^5(^{6}S)4s a^{7}S$_3$. The metastable levels cannot decay to a lower level by electric dipole radiation. The majority of these levels lie below the lowest odd-parity term, which in Mn II is the 3d^5(^{6}S)4p z^{7}P term near 38,500 cm^{-1} (Liggins et al. 2021). A partial energy level diagram of Mn II is given in Figure 1 showing the ground level and the lower metastable levels. The ground state and the low-lying terms belong to the even 3d^5(^{6}S)4s, 3d^5(^{4}G)4s, 3d^5(^{4}P)4s, 3d^5(^{4}D)4s, and 3d^6 electronic configurations. The most astrophysically important forbidden lines belong to quintet levels in these configurations and have been observed in the spectrum of η Carinae (Hartman et al. 2004).

Observed wavenumbers and uncertainties of about 1400 allowed (E1) transitions in Mn II were used with the least-squares fitting program LOPT (Kramida 2011) to optimize the energy level values. The wavenumber uncertainties for these lines were typically of order 0.001 cm^{-1}, with the strongest transitions observed in the visible and UV regions. These strong lines often exhibit HFS that could be fitted in order to reduce the uncertainties by up to an order of magnitude. Each line was weighted in the optimization by the reciprocal of the square of the line's wavenumber uncertainty. This enabled all observed transitions to the level of interest to be included while avoiding any deterioration to the level fit from poorer measurements.

Parity-forbidden transitions were attributed to magnetic dipole (M1) and/or electric quadrupole (E2) radiation according to the selection rules given in Table 1. Vacuum Ritz wavenumbers were derived for these transitions using optimized energy levels. This resulted in a total of 1130 parity-forbidden transitions

within a wavelength range of 237 nm to 170 μm, corresponding to a wavenumber range of 42,125 cm^{-1} to 58 cm^{-1}.

The uncertainties in the calculated wavenumbers were taken from the covariance matrix in LOPT and were combined in quadrature with an upper estimate for the calibration uncertainty of 5×10^{-8} times the wavenumber. Calculated Ritz wavelengths, λ_{vac}, derived from the vacuum wavenumber, σ, then carry the related uncertainty

$$\Delta\lambda_{vac} = 10^7 \times \frac{\Delta\sigma}{\sigma^2}, \quad (1)$$

where λ_{vac} is in nm and σ is in cm^{-1}.

Air wavelengths were derived from the Ritz wavenumbers using the five-parameter formula of Peck & Reeder (1972), which we consider to be the most reliable over the range 2 μm to 200 nm. The refractive index of air has been widely investigated by, for example, Edlén (1966), Peck & Reeder (1972), Birch & Downs (1994), Ciddor (1996), and Bönsch & Potulski (1998), but the differences between these formulae increase in the infrared region. These differences are largely due to the change in the constituents of "standard air" between the time of the older measurements and the more recent ones. It is recommended, therefore, that the vacuum wavelengths and wavenumbers be used where possible and air wavelengths below 2 μm be calculated from these using the index deemed most suitable for that of the observations of interest.

4. Transition Probability Calculations

Spectra of iron-group elements are generally too complex to use high-quality MCHF/MCDF and similar ab initio methods to calculate transition probabilities for forbidden lines. Although a few such calculations have been performed, semi-empirical methods using the Cowan code (Cowan 1981) are usually used, taking experimentally measured energy level values. Here the measured energy levels compiled in KS have been used. Although these are less accurate than the new energy levels measured by Liggins et al. (2021), these were available at the time of the calculations, and the differences in energy level values between these two publications are insignificant in the context of semi-empirical calculations, where energy level values calculated can differ from experimentally measured values by many orders of magnitude compared with the uncertainty of the energy levels themselves, and the calculated transition probabilities themselves are unaffected.

Although methods have been developed to estimate the uncertainties of ab initio calculations, methods for estimating the uncertainties of semi-empirical calculations are scarce. In this paper, we use two methods to assess these uncertainties. The first method, described in Section 6.1, uses the Monte Carlo technique of Kramida (2014) to estimate the uncertainties from the standard deviation of up to 100 trials. The second method compares three different calculations using the Cowan Code, each having different sets of input configurations. The first set of calculations was performed at the Université de Mons (UMONS). This calculation included a limited set of valence configurations and a set of core-excited configurations. The second set of calculations was performed at NIST and included a more extensive set of valence configurations with no core-excited configurations. The third set of calculations was taken from the Kurucz website.[5] The differences between the calculations provides an estimate of the sensitivity of the calculations to the input parameters.

4.1. Calculations at Université de Mons

Transition probabilities for [Mn II] lines were computed using the pseudo-relativistic Hartree–Fock (HFR) approach implemented in the Cowan suite of computer codes (Cowan 1981). The following configurations were explicitly included in the physical model: $3d^5 4s$, $3d^5 5s$, $3d^6$, $3d^4 4s^2$, $3d^5 4d$, $3d^5 5d$, $3d^4 4p^2$, $3d^4 4d^2$, $3d^4 4s4d$, $3s3d^6 4s$, $3s3d^7$, and $3s3d^5 4s^2$. In order to minimize the discrepancies between computed and experimental energy levels, the HFR method was used in combination with a well-known least-squares fitting of the radial parameters. This fitting procedure was applied to $3d^5 4s$ and $3d^6$ with the experimental energy levels compiled by Kramida & Sansonetti (2013) (KS), by considering, as adjustable parameters, the average energies (E_{av}), the Slater electrostatic integrals (F^k, G^k, R^k), the spin–orbit parameters (ζ_{nl}), and the effective interaction parameters (α, β) associated with these two configurations. The ab initio HFR values for all the Slater integrals related to configurations other than $3d^5 4s$ and $3d^6$ were scaled down by a factor of 0.85 as recommended by Cowan (1981), while the ab initio values of all the spin–orbit integrals, computed by the Blume Watson method (Blume & Watson 1962), were used without scaling. The average deviation, specifically the arithmetic mean of the absolute difference, between computed and experimental levels is 241 cm^{-1}.

This calculation was repeated twice at NIST, first with exactly the same configurations and second with all the configuration interaction (CI) integrals involving $3d^4 4d^2$, $3s3d^6 4s$, $3s3d^7$, and $3s3d^5 4s^2$ set to zero. This was done to investigate the importance of core-excited configurations on the forbidden line transition probabilities.

4.2. Calculations of Kurucz

These calculations included the following configurations: $3d^6$, $3d^5 n$d ($n = 4\ldots12$), $3d^4 4sn$d ($n = 4\ldots9$), $3d^5 ns$ ($n = 4\ldots12$), $3d^4 4sns$ ($n = 4\ldots9$), $3d^5 ng$ ($n = 5\ldots9$), $3d^4 4sng$ ($n = 5\ldots9$), $3d^5 ni$ ($n = 7\ldots9$), $3d^5 9l$, $3d^5 4s9l$, and $3d^4 4p^2$. All experimentally known levels included in the KS compilation were used for the least squares fitting, as were 53 even-parity levels from Castelli et al. (2015) derived from astrophysical spectra. The average deviation between the experimental and fitted levels is 30 cm^{-1} from 272 even-parity levels, with deviations of 46 cm^{-1} from 32 levels in the $3d^6$ configuration and 68 cm^{-1} for 62 levels of the $3d^5 4s$ configuration.

4.3. Calculations at NIST

These are similar to the Kurucz calculations, but with a smaller set of configurations: $3d^6$, $3d^5 n$d ($n = 4$–8), $3d^4 4s4d$, $3d^5 ns$ ($n = 4$–8), $3d^4 4sns$ ($n = 4$–5), and $3d^4 4p^2$. All of the experimentally known levels in the KS compilation were fitted except for one $J = 4$ level from Castelli et al. (2015) at 113,199.572 cm^{-1}. The average deviation between the experimental and fitted levels is 132 cm^{-1} (108 cm^{-1} for $3d^6$ and 95 cm^{-1} for $3d^5 4s$).

5. Results

Atomic parameters for 63 parity-forbidden [Mn II] transitions from the a ^{5}P, a ^{5}D, a ^{5}G, b ^{5}D terms with branching fractions >0.01 are presented in Table 2. Forbidden lines from

[5] Files gam2501e.pos and gaq2501e.pos, dated 2016 September 3, downloaded from http://kurucz.harvard.edu/atoms/2501/.

Table 2
[Mn II] Lines from The a^5S, a^5D, a^5P, a^5G, b^5D Levels Sorted by Wavenumber

Air λ[a] (nm)	Vacuum λ[a] (nm)	Unc.[b] (nm)	Wavenumber (cm^{-1})	Unc.[b] (cm^{-1})	Energy Levels		Energy Level Values (cm^{-1})		BF[c]	A (s^{-1})	Unc.[b]	Type
					Lower	Upper	Lower	Upper				
⋯	170448.0	2.1	58.6689	0.0007	a $^5D_1$	a $^5D_0$	14901.1979	14959.8668	0.01	3.28E-05	1%	M1
⋯	83333.1	0.3	120.0004	0.0005	a $^5D_2$	a $^5D_1$	14781.1975	14901.1979	0.07	1.64E-04	1%	M1
⋯	53370.67	0.11	187.3688	0.0004	a $^5D_3$	a $^5D_2$	14593.8287	14781.1975	0.18	4.27E-04	1%	M1
⋯	37317.06	0.08	267.9739	0.0006	a $^5D_4$	a $^5D_3$	14325.8547	14593.8287	0.29	6.70E-04	1%	M1
⋯	3487.9431	0.0024	2867.0193	0.0019	a $^5P_1$	b $^5D_0$	29951.4394	32818.4587	0.07	3.52E-02	30%	M1
⋯	3465.8382	0.0021	2885.3049	0.0017	a $^5P_1$	b $^5D_1$	29951.4394	32836.7444	0.02	1.19E-02	30%	M1
⋯	3450.2118	0.0015	2898.3727	0.0013	a $^5P_3$	b $^5D_4$	29889.5380	32787.9107	0.03	1.54E-02	30%	M1
⋯	3427.8331	0.0018	2917.2949	0.0015	a $^5P_2$	b $^5D_1$	29919.4495	32836.7444	0.03	1.56E-02	30%	M1
⋯	3401.6843	0.0016	2939.7202	0.0014	a $^5P_2$	b $^5D_2$	29919.4495	32859.1697	0.02	9.36E-03	30%	M1
⋯	3367.4209	0.0017	2969.6317	0.0015	a $^5P_3$	b $^5D_2$	29889.5380	32859.1697	0.01	6.63E-03	30%	M1
⋯	2060.63911	0.00020	4852.8633	0.0005	a $^5S_2$	a $^5D_4$	9472.9914	14325.8547	0.97	1.25E-03	30%	E2
1952.27266	1952.80566	0.00015	5120.8373	0.0004	a $^5S_2$	a $^5D_3$	9472.9914	14593.8287	0.70	1.63E-03	30%	E2
1883.36137	1883.87561	0.00011	5308.2061	0.0003	a $^5S_2$	a $^5D_2$	9472.9914	14781.1975	0.81	1.93E-03	30%	E2
1841.72620	1842.22910	0.00016	5428.2065	0.0005	a $^5S_2$	a $^5D_1$	9472.9914	14901.1979	0.93	2.16E-03	30%	E2
1822.03335	1822.53089	0.00022	5486.8754	0.0006	a $^5S_2$	a $^5D_0$	9472.9914	14959.8668	0.99	2.27E-03	30%	E2
1055.34360	1055.63276	0.00011	9472.9914	0.0009	a $^7S_3$	a $^5S_2$	0.0000	9472.9914	1.00	1.46E-06	80%	M1
791.57775	791.79551	0.00011	12629.5236	0.0018	a $^5D_0$	a $^5G_2$	14959.8668	27589.3904	0.34	2.89E-02	30%	E2
787.97258	788.18935	0.00009	12687.3066	0.0014	a $^5D_1$	a $^5G_3$	14901.1979	27588.5045	0.40	3.50E-02	30%	E2
787.91756	788.13432	0.00011	12688.1925	0.0018	a $^5D_1$	a $^5G_2$	14901.1979	27589.3904	0.48	4.02E-02	30%	E2[d]
780.89071	781.10557	0.00010	12802.3667	0.0016	a $^5D_2$	a $^5G_4$	14781.1975	27583.5642	0.52	4.78E-02	30%	E2[d]
780.58948	780.80427	0.00008	12807.3071	0.0014	a $^5D_2$	a $^5G_3$	14781.1975	27588.5045	0.47	4.06E-02	30%	E2[d]
780.53549	780.75026	0.00010	12808.1929	0.0017	a $^5D_2$	a $^5G_2$	14781.1975	27589.3904	0.16	1.34E-02	80%	E2[d]
770.35958	770.57160	0.00010	12977.3794	0.0018	a $^5D_3$	a $^5G_5$	14593.8287	27571.2080	0.72	6.90E-02	30%	E2[d]
769.62679	769.83861	0.00009	12989.7356	0.0016	a $^5D_3$	a $^5G_4$	14593.8287	27583.5642	0.42	3.79E-02	30%	E2
769.33419	769.54593	0.00008	12994.6759	0.0014	a $^5D_3$	a $^5G_3$	14593.8287	27588.5045	0.12	1.08E-02	80%	E2
769.28175	769.49348	0.00010	12995.5617	0.0017	a $^5D_3$	a $^5G_2$	14593.8287	27589.3904	0.02	1.36E-03	80%	E2
756.14278	756.35097	0.00010	13221.3753	0.0018	a $^5D_4$	a $^5G_6$	14325.8547	27547.2300	1.00	1.03E-01	30%	E2[d]
754.77393	754.98175	0.00010	13245.3533	0.0018	a $^5D_4$	a $^5G_5$	14325.8547	27571.2080	0.29	2.75E-02	30%	E2[d]
754.07048	754.27810	0.00009	13257.7095	0.0016	a $^5D_4$	a $^5G_4$	14325.8547	27583.5642	0.06	5.44E-03	80%	E2
697.84616	698.03863	0.00005	14325.8547	0.0010	a $^7S_3$	a $^5D_4$	0.0000	14325.8547	0.03	3.49E-05	80%	E2[d]
685.03212	685.22115	0.00005	14593.8287	0.0010	a $^7S_3$	a $^5D_3$	0.0000	14593.8287	0.02	4.00E-05	80%	E2[d]
676.34849	676.53517	0.00004	14781.1975	0.0010	a $^7S_3$	a $^5D_2$	0.0000	14781.1975	0.01	2.79E-05	80%	E2
668.28333	668.46785	0.00006	14959.5827	0.0013	a $^5D_0$	a $^5P_2$	14959.8668	29919.4495	0.03	1.85E-02	80%	E2
665.67266	665.85647	0.00005	15018.2516	0.0012	a $^5D_1$	a $^5P_2$	14901.1979	29919.4495	0.07	4.56E-02	30%	E2[d]
664.25773	664.44116	0.00007	15050.2415	0.0016	a $^5D_1$	a $^5P_1$	14901.1979	29951.4394	0.05	1.37E-02	80%	E2
661.70332	661.88606	0.00005	15108.3405	0.0012	a $^5D_2$	a $^5P_3$	14781.1975	29889.5380	0.03	2.46E-02	80%	E2
660.39585	660.57825	0.00005	15138.2520	0.0012	a $^5D_2$	a $^5P_2$	14781.1975	29919.4495	0.07	4.17E-02	30%	E2
659.00325	659.18527	0.00007	15170.2419	0.0015	a $^5D_2$	a $^5P_1$	14781.1975	29951.4394	0.24	6.92E-02	30%	E2
653.59755	653.77811	0.00005	15295.7093	0.0012	a $^5D_3$	a $^5P_3$	14593.8287	29889.5380	0.10	7.68E-02	30%	E2[d]
650.96309	651.14295	0.00007	15357.6108	0.0016	a $^5D_3$	a $^5P_1$	14593.8287	29951.4394	0.56	1.61E-01	30%	E2[d]
642.34389	642.52143	0.00005	15563.6832	0.0012	a $^5D_4$	a $^5P_3$	14325.8547	29889.5380	0.18	1.49E-01	30%	E2[d]
641.11174	641.28895	0.00005	15593.5948	0.0012	a $^5D_4$	a $^5P_2$	14325.8547	29919.4495	0.22	1.40E-01	30%	E2[d]
558.52590	558.68098	0.00004	17899.3029	0.0014	a $^5D_0$	b $^5D_2$	14959.8668	32859.1697	0.20	1.08E-01	30%	E2
557.39723	557.55201	0.00004	17935.5465	0.0014	a $^5D_1$	b $^5D_1$	14901.1979	32836.7444	0.33	1.75E-01	30%	E2
556.75975	556.91436	0.00005	17956.0822	0.0015	a $^5D_1$	b $^5D_3$	14901.1979	32857.2801	0.15	8.35E-02	30%	E2
556.70117	556.85576	0.00004	17957.9718	0.0013	a $^5D_1$	b $^5D_2$	14901.1979	32859.1697	0.19	1.02E-01	30%	E2
555.19425	555.34843	0.00003	18006.7132	0.0010	a $^5D_2$	b $^5D_4$	14781.1975	32787.9107	0.06	3.34E-02	80%	E2
554.25396	554.40789	0.00005	18037.2612	0.0015	a $^5D_2$	b $^5D_0$	14781.1975	32818.4587	0.93	4.91E-01	30%	E2
553.69263	553.84642	0.00004	18055.5469	0.0014	a $^5D_2$	b $^5D_1$	14781.1975	32836.7444	0.30	1.60E-01	30%	E2
553.06359	553.21721	0.00004	18076.0826	0.0014	a $^5D_2$	b $^5D_3$	14781.1975	32857.2801	0.36	1.94E-01	30%	E2
553.00578	553.15939	0.00004	18077.9722	0.0012	a $^5D_2$	b $^5D_2$	14781.1975	32859.1697	0.02	8.57E-03	80%	E2
549.47661	549.62927	0.00003	18194.0821	0.0010	a $^5D_3$	b $^5D_4$	14593.8287	32787.9107	0.31	1.73E-01	30%	E2
548.00572	548.15799	0.00004	18242.9157	0.0014	a $^5D_3$	b $^5D_1$	14593.8287	32836.7444	0.31	1.61E-01	30%	E2
547.38953	547.54163	0.00004	18263.4515	0.0015	a $^5D_3$	b $^5D_3$	14593.8287	32857.2801	0.10	5.55E-02	80%	E2
547.33290	547.48499	0.00004	18265.3410	0.0013	a $^5D_3$	b $^5D_2$	14593.8287	32859.1697	0.46	2.42E-01	30%	E2
541.50095	541.65148	0.00003	18462.0560	0.0010	a $^5D_4$	b $^5D_4$	14325.8547	32787.9107	0.59	3.27E-01	30%	E2
539.47391	539.62390	0.00004	18531.4254	0.0015	a $^5D_4$	b $^5D_3$	14325.8547	32857.2801	0.34	1.86E-01	30%	E2
539.41890	539.56888	0.00004	18533.3150	0.0013	a $^5D_4$	b $^5D_2$	14325.8547	32859.1697	0.08	4.37E-02	80%	E2
489.66207	489.79880	0.00003	20416.5466	0.0012	a $^5S_2$	a $^5P_3$	9472.9914	29889.5380	0.02	1.82E-02	80%	M1
488.18192	488.31825	0.00004	20478.4480	0.0015	a $^5S_2$	a $^5P_1$	9472.9914	29951.4394	0.15	4.22E-02	80%	M1
334.469066	334.565225	0.000017	29889.5380	0.0015	a $^7S_3$	a $^5P_3$	0.0000	29889.5380	0.66	5.33E-01	80%	M1

Table 2
(Continued)

Air λ[a] (nm)	Vacuum λ[a] (nm)	Unc.[b] (nm)	Wavenumber (cm^{-1})	Unc.[b] (cm^{-1})	Energy Levels		Energy Level Values (cm^{-1})		BF[c]	A (s^{-1})	Unc.[b]	Type
					Lower	Upper	Lower	Upper				
334.134674	334.230748	0.000017	29919.4495	0.0015	a $^7S_3$	a $^5P_2$	0.0000	29919.4495	0.60	3.75E-01	80%	M1
304.258029	304.346555	0.000016	32857.2801	0.0017	a $^7S_3$	b $^5D_3$	0.0000	32857.2801	0.02	1.27E-02	80%	M1

Notes.
[a] Wavelength. Air wavelengths calculated in the range 200–2000 nm using the five-parameter formula of Peck & Reeder (1972). Energy levels are from Liggins et al. (2021). Note that the differences of the energy levels may not match the Ritz wavelengths and wavenumbers due to small differences in the rounding of the values.
[b] Uncertainty of the previous column (previous two columns for wavelength).
[c] Branching fraction (ratio of the transition probability to the sum of the transition probabilities from all decays from that level.
[d] Line observed in the spectrum of η Carinae (Hartman et al. 2004).

(This table is available in machine-readable form.)

Table 3
[Mn II] Lines Sorted by Wavenumber

Air[a] Wavelength (nm)	Vacuum Wavelength (nm)	Unc.[b] (nm)	Wavenumber (cm^{-1})	Unc.[b] (cm^{-1})	Transition		Energy (cm^{-1})		BF
					Lower Level	Upper Level	Lower Level	Upper Level	
1271.2068	1271.5545	0.0007	7864.389	0.004	3d5.(4P).4s.b3P.2	3d5.(2D).4s.c3D.1	36274.6499	44139.039	0.0030
1261.3949	1261.7399	0.0010	7925.563	0.006	3d5.(4G).4s.a3G.3	3d5.(2I).4s.a3I.5	33278.802	41204.366	0.0370
1260.8788	1261.2238	0.0004	7928.8070	0.0023	3d5.(4P).4s.a5P.2	3d6.a3D.2	29919.4495	37848.2565	0.0005
1258.8211	1259.1655	0.0008	7941.768	0.005	3d5.(4G).4s.a3G.4	3d5.(2I).4s.a3I.6	33248.7026	41190.471	0.0354
1258.7059	1259.0500	0.0011	7942.497	0.007	3d6.a3P.2	3d6.a3D.1	29869.430	37811.927	0.0510
1256.6224	1256.9662	0.0009	7955.663	0.006	3d5.(4G).4s.a3G.4	3d5.(2I).4s.a3I.5	33248.7026	41204.366	0.0086
1252.9744	1253.3172	0.0008	7978.826	0.005	3d6.a3P.2	3d6.a3D.2	29869.430	37848.2565	0.1587
1252.4637	1252.8063	0.0008	7982.080	0.005	3d6.a3P.2	3d6.a3D.3	29869.430	37851.5100	0.1654
1252.1062	1252.4488	0.0018	7984.359	0.012	3d5.(2H).4s.a1H.5	3d6.c1G.4	51553.094	59537.452	0.0032

A_{tot} (s^{-1})	Unc.[b]	Type[c]	A(M1)(s^{-1})			A(E2)(s^{-1})			A(M1+E2) (s^{-1})		
			NIST	Mons	Kurucz	NIST	Mons	Kurucz	NIST	Mons	Kurucz
6.02E-03	80%	M1	5.70E-03	6.30E-03	6.06E-03	…	…	…			
1.80E-03	30%	E2	…	…	…	1.61E-03	2.15E-03	1.65E-03			
4.57E-05	80%	M1*	1.12E-04	4.51E-06	2.06E-05	…	…	…			
1.87E-03	30%	E2	…	…	…	1.70E-03	2.20E-03	1.70E-03			
5.61E-03	80%	M1+E2	4.94E-03	5.32E-03	4.78E-03	4.84E-04	6.97E-04	5.97E-04	5.42E-03	6.02E-03	5.38E-03
4.21E-04	80%	M1+E2	8.38E-05	5.78E-05	7.42E-05	3.14E-04	4.06E-04	3.26E-04	3.98E-04	4.64E-04	4.00E-04
1.48E-02	70%	M1+E2	1.34E-02	1.33E-02	1.17E-02	1.60E-03	2.40E-03	2.13E-03	1.50E-02	1.57E-02	1.38E-02
1.61E-02	70%	M1+E2	1.25E-02	1.25E-02	1.09E-02	3.13E-03	4.75E-03	4.41E-03	1.56E-02	1.73E-02	1.53E-02
1.03E-02	30%	E2	…	…	…	9.72E-03	1.07E-02	1.06E-02			

Notes.
[a] Calculated for wavelengths in the range 200–2000 nm using the five-parameter formula of Peck & Reeder (1972). Energy levels are from Liggins et al. (2021). Note that the differences of the energy levels may not match the Ritz wavelengths and wavenumbers due to small differences in the rounding of the values.
[b] Uncertainty of the previous column (previous two columns for wavelength).
[c] Type of transition. Flags indicate: *Transition probabilities from the three calculations do not agree within the uncertainties. #Standard deviation of the MC calculations is larger than 80%.

(This table is available in its entirety in machine-readable form.)

these terms are most likely to be seen in spectra of astrophysical objects and 20 of them have been observed in the spectrum of η Carinae by Hartman et al. (2004). Calculated Ritz air and vacuum wavelengths are provided in columns 1 and 2, wavenumbers in column 4, and their associated uncertainties in columns 3 and 5, respectively. The abbreviated designations for the lower and upper levels of the transitions are given in columns 6 and 7, and the energy values for these, in 8 and 9. The calculated branching fraction (i.e., ratio of the transition probability to the sum of transition probabilities for all decays from the upper level) in column 10 and sum of the M1 and E2 transition probabilities, A, in column 11 are averages of the three calculations. The estimated transition probability uncertainty in column 12 is derived from the Monte Carlo calculations described in Section 6.1.

The parameters for all of the calculated transitions, 1130 transitions, are given in Table 3. In addition to the information given in Table 2, results from the three different calculations

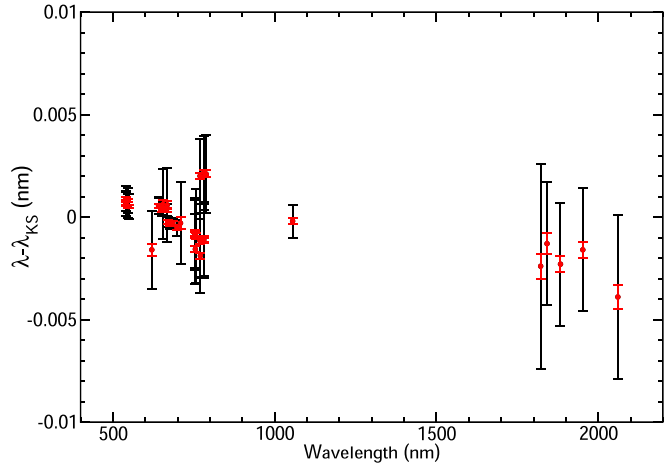

Figure 2. Difference between [Mn II] Ritz wavelengths in this work, λ, and previous Ritz wavelengths, λ_{KS}, taken from Kramida & Sansonetti (2013). The red and black error bars show the uncertainties in the new and previous Ritz wavelength values respectively.

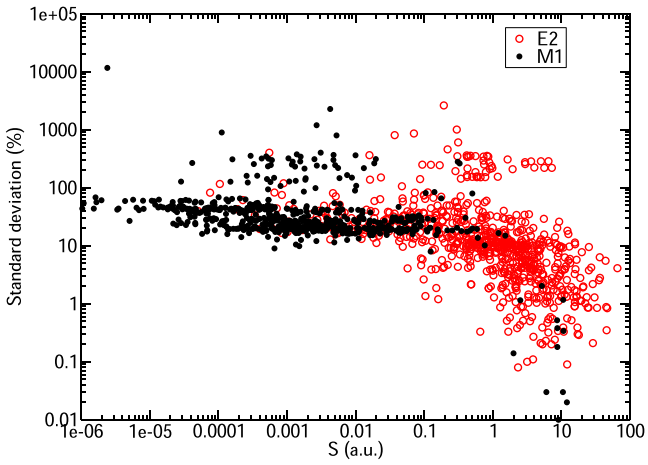

Figure 3. Monte Carlo simulation for M1 (closed black circles) and E2 transitions (open red circles) in Mn II using the NIST set of configurations as a function of S in atomic units defined by Equations (3) and (2). The standard deviation is based on 100 trials, randomly varying the Slater parameters around the initial values.

are given, separated out according to the type (M1 or E2) of transition. The transition is given as a pure M1 or E2 transition if the smaller component does not exceed 10% of the total, otherwise it is given as M1+E2. An asterisk is given in column 13 if one or more of the three calculations disagrees with the other two. Lines where the Monte Carlo simulations indicate that the uncertainties may be underestimated by the global uncertainty estimates are marked with a hash mark in column 13.

Figure 2 shows the difference, $\Delta\lambda = \lambda - \lambda_{KS}$, between the Ritz wavelengths of this work and from KS. The KS Ritz wavelengths were primarily based on the older grating measurements of Iglesias & Velasco (1964) whereas those of this work are based on more accurate Fourier-transform spectroscopy measurements (Liggins et al. 2021). The error bars represent the Ritz wavelength uncertainties as given in this work (red) and by KS (black). The differences between the KS and new work Ritz wavelengths are within the uncertainties of the KS wavelengths. It can be seen that for newly derived wavelengths there is typically a decrease in the uncertainty by at least an order of magnitude compared with previous Ritz wavelengths.

6. Comparisons of the Calculations and Estimates of Uncertainties

6.1. Monte Carlo Calculations

A Monte Carlo technique was used to assess the uncertainties of the NIST and Mons calculations using the method of Kramida (2014). This method repeats the calculations up to 100 times, randomly varying the input Slater parameters around the initial values, the spread of these variations being defined by the standard deviations of the least-squares fitting of the Slater parameters. The standard deviation of the transition probabilities calculated with those varied parameters provides an estimate of the statistical uncertainty of the calculation.

Figure 3 shows the results of the Monte Carlo simulations for 642 M1 transitions and 750 E2 transitions in Mn II, plotted as a function of the line strength S of the NIST calculations in atomic units (a.u.) (Drake 1996 chap. 10):

$$a_0^4 e^2 = 2.013 \times 10^{-79} \mathrm{m}^4\mathrm{C}^2 \quad (2)$$

for electric quadrupole, and

$$\mu_B^2 = 8.601 \times 10^{-47} \mathrm{J}^2\,\mathrm{T}^{-2} \quad (3)$$

for magnetic dipole, where a_0 is the Bohr radius, e is the elementary charge, and μ_B is the Bohr magneton. The standard deviations of the transition probabilities show a clear dependence on the line strength S and the type of transition (M1 or E2). Strong M1 transitions in general have a lower standard deviation than the strong E2 transitions, and transitions with $S > 2$ a.u. have standard deviations of less than 1%. The majority of lines with $0.01 < S < 2$ a.u. have standard deviations between 15% and 30%, although a few exceed 200%. The standard deviation of weaker M1 and E2 transitions approaches 80%, again with some outliers of much larger standard deviation. The figure suggests the following average estimates for the uncertainties of the NIST calculations:

M1, $S > 2$ a.u.: 1%
M1, $0.01 < S < 2$ a.u. 30%
M1, $S < 0.01$ a.u. 80%
E2, $S > 2$ a.u. 30%
E2, $S < 2$ a.u. 80%.

These values are used to set the uncertainties of the transition probabilities given in Table 2.

6.2. Influence of Core-excited Configurations

A comparison of the two calculations using the Mons set of configurations is given in Figure 4, for M1 transitions (left) and E2 transitions (right). The ratio of the A values is plotted as a function of the line strength in either the calculation with the core-excited levels included (S_{core}), or against the line strength with the CI integrals for the core-excited configurations set to zero ($S_{no\ core}$).

By comparing the distribution of points for each data set on the plots, it is possible to estimate which calculation is likely to have a higher accuracy. If the ratio of an inaccurate calculation and an accurate calculation is plotted against S of the less accurate calculation, the distribution of points is likely to display a regular pattern of increasing scatter with decreasing

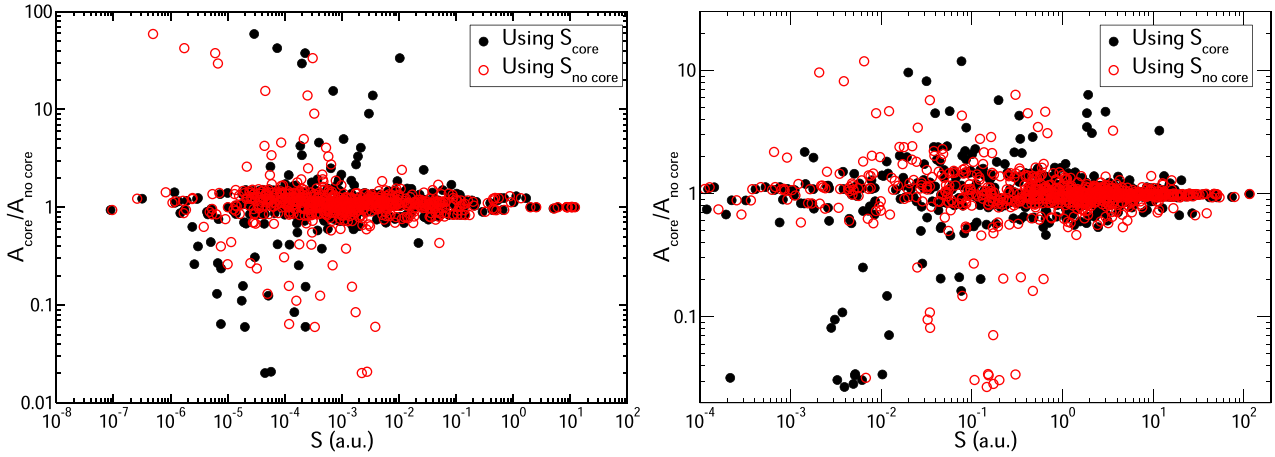

Figure 4. Left: comparison of calculated transition probabilities for M1 transitions of Mn II, including (black, $S_{\rm core}$) and excluding (red, $S_{\rm no\ core}$) core-excited configurations. Right: same as left, but for E2 transitions. The line strength, S, is in atomic units defined by Equations (2) and (3).

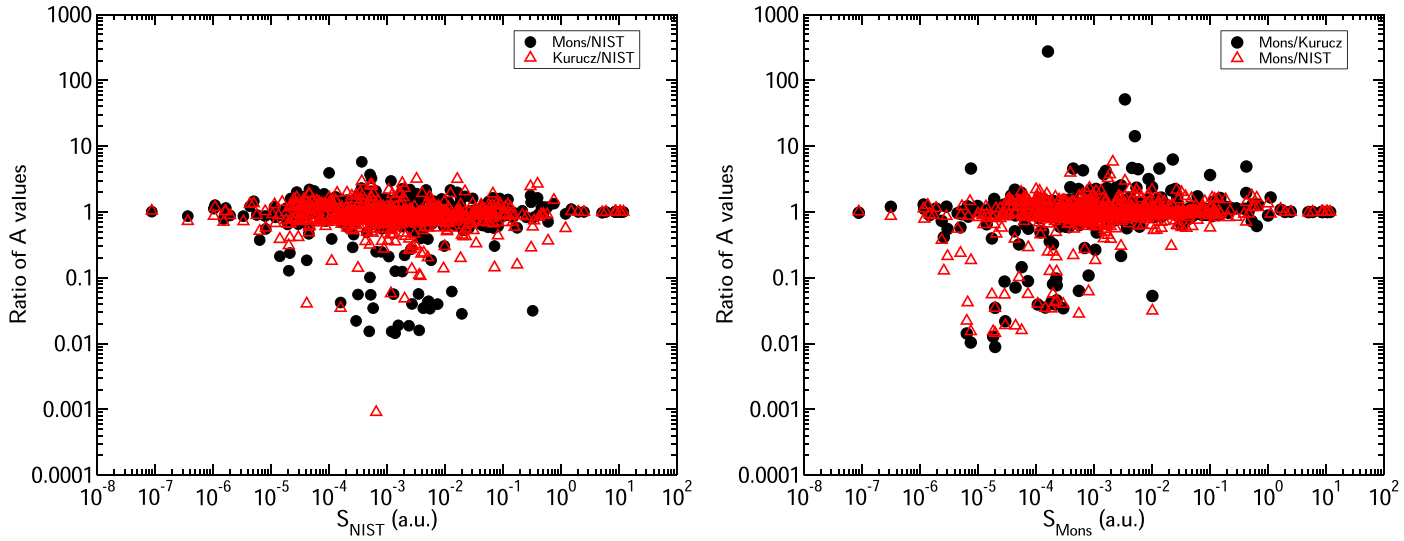

(a) (b)

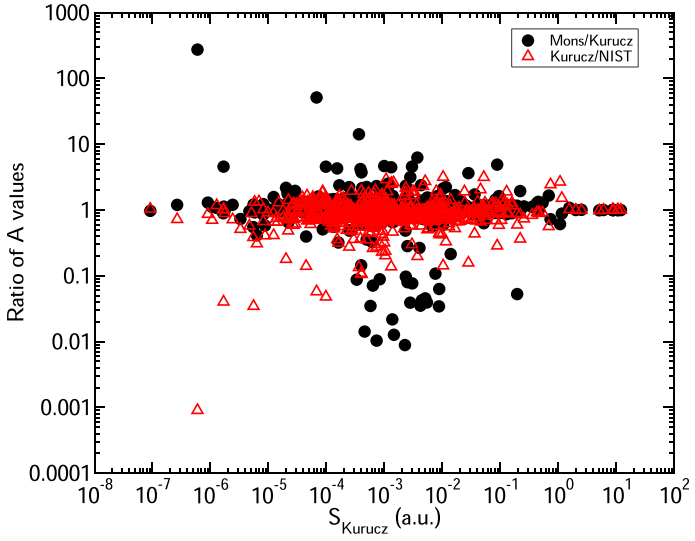

(c)

Figure 5. Comparison of M1 transitions of Mn II for the three calculations (a) as a function of $S_{\rm NIST}$ from NIST, (b) as a function of $S_{\rm Mons}$ from Université de Mons, and (c) as a function of $S_{\rm Kurucz}$ from Kurucz. The line strength S is in atomic units defined by Equation (3).

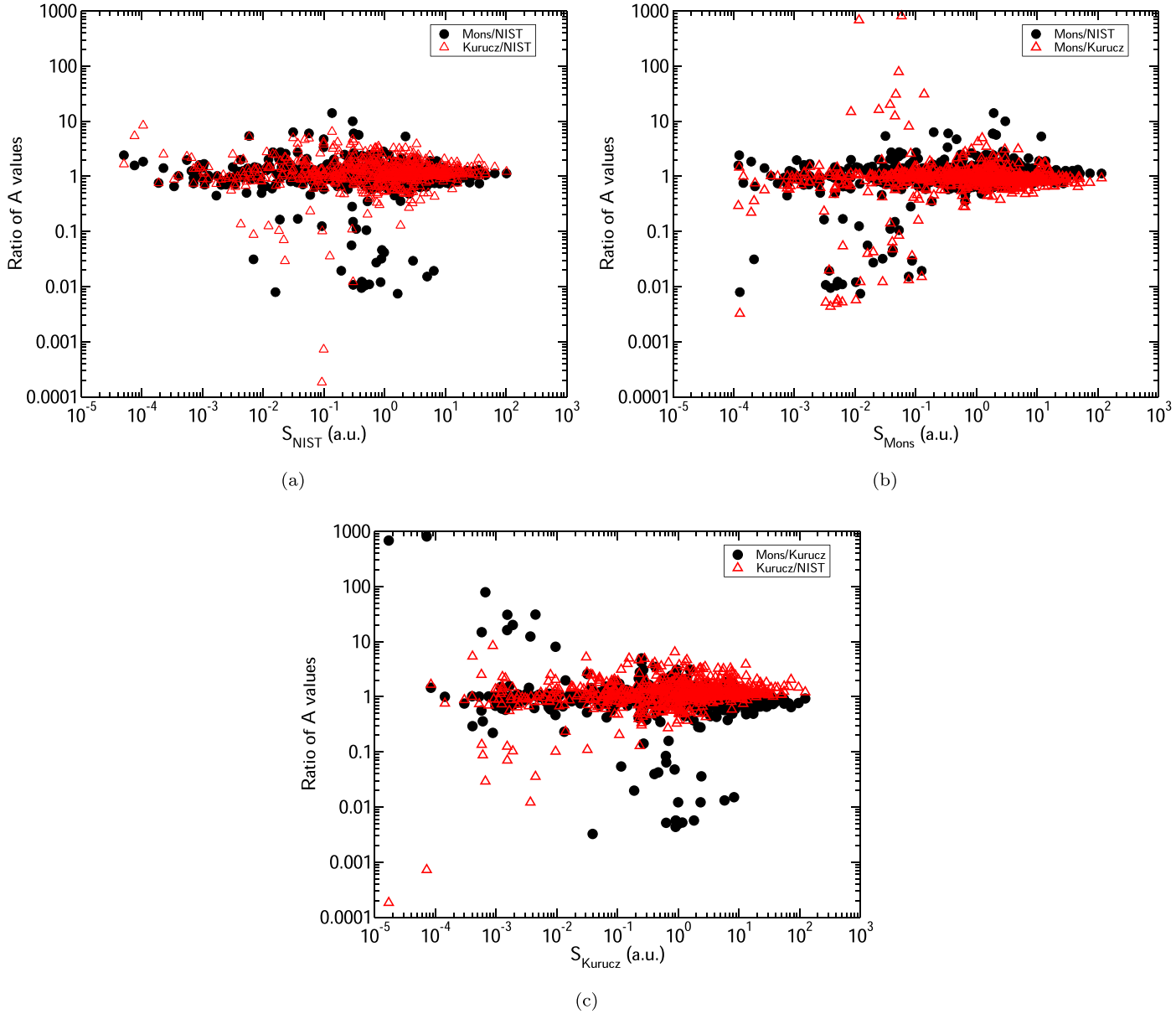

Figure 6. Comparison of E2 transitions of Mn II for the three calculations (a) as a function of line strength $S_{\rm NIST}$ from NIST, (b) as a function of line strength $S_{\rm Mons}$ from Université de Mons, and (c) as a function of line strength $S_{\rm Kurucz}$ from Kurucz. The line strength S is in atomic units defined by Equation (2).

line strength, reflecting the intrinsic inaccuracy of the calculated S values. If, however, the ratio is plotted against S of the more accurate calculation, the ratio will be unchanged, but the points will move to higher or lower values of the line strength, causing irregularly large deviations to appear for large line strengths.

These figures show that the inclusion of core-excited configurations does not significantly change the calculation as the distribution of the scatter with respect to line strength does not change significantly between the two calculations. The accuracy of the calculations of M1 transitions is not significantly improved by the inclusion of the core-excited configurations and is slightly improved for E2 transitions.

6.3. Comparison of the Three Calculations

Figure 5 compares the results of the three calculations for M1 transitions in Mn II, as a function of S, calculated by NIST (a), Université de Mons (b), and Kurucz (c). The three calculations generally agree within the standard uncertainties determined by the Monte Carlo calculations in Section 6.1. Figure 6 shows similar figures for E2 transitions of Mn II, with the majority of values agreeing within the uncertainties from Section 6.1. We have thus adopted the Monte Carlo results as estimates of the uncertainties of the transition probabilities in Tables 2 and 3.

7. Conclusion

We report a comprehensive list of accurate Ritz wavelengths and calculated transition probabilities for parity-forbidden lines of [Mn II]. These wavelengths are calculated from optimized energy levels of Mn II from an extensive spectral analysis. The transition probabilities are derived using three different calculations using the Cowan code. Uncertainties of the transition probabilities have been estimated using Monte Carlo techniques

and by the agreement of the three calculations. A subset of 56 lines is potentially detectable in astrophysical plasmas, of which 20 have been observed in the spectrum of η Carinae. The atomic parameters in this paper are useful in the study and diagnostics of nebulae and other low-density astrophysical plasmas.

This work was supported by the STFC (UK) awards ST/K001051/1 and ST/N000838/1 and NASA agreements NNH14AY78I and NNH17AE08I. P.Q. is Research Director of the Belgian National Fund for Scientific Research (F.R.S.-FNRS), whose financial support is gratefully acknowledged.

ORCID iDs

Florence S. Liggins https://orcid.org/0000-0003-3448-4704
Juliet C. Pickering https://orcid.org/0000-0003-2879-4140
Gillian Nave https://orcid.org/0000-0002-1718-9650
Alexander Kramida https://orcid.org/0000-0002-0788-8087
Sébastien Gamrath https://orcid.org/0000-0002-9115-590X
Pascal Quinet https://orcid.org/0000-0002-3937-2640

References

Birch, K. P., & Downs, M. J. 1994, Metro, 31, 315
Blackwell-Whitehead, R. J. 2003, PhD thesis, Imperial College London
Blume, M., & Watson, R. E. 1962, RSPSA, 270, 127
Bönsch, G., & Potulski, E. 1998, Metro, 35, 133
Castelli, F., Kurucz, R. L., & Cowley, C. R. 2015, A&A, 580, A10
Ciddor, P. E. 1996, ApOpt, 35, 1566
Cowan, R. 1981, The Theory of Atomic Structure and Spectra (Berkeley, CA: Univ. California Press)
Drake, G. W. F. (ed.) 1996, Atomic, Molecular, and Optical Physics Handbook (Woodbury, NY: AIP Press) Chap. 10
Edlén, B. 1966, Metro, 2, 71
Hartman, H., Gull, T., Johansson, S., Smith, N. & HST Eta Carinae Treasury Project Team 2004, A&A, 419, 215
Iglesias, L., & Velasco, R. 1964, Publ. Inst. Opt. Madrid (Daza de Valdés), 23, 1
Kling, K., & Griesmann, U. 2000, ApJ, 531, 1173
Kramida, A. 2014, Atoms, 2, 86
Kramida, A., & Sansonetti, J. 2013, ApJS, 205, 14
Kramida, A. E. 2011, CoPhC, 182, 4419
Liggins, F. S. 2017, PhD thesis, Imperial College London, doi:10.25560/59134
Liggins, F. S., Pickering, J. C., Nave, G., Ward, J. W., & Tchang-Brillet, W.-Ü. L. 2021, ApJS, 252, 10
Nave, G., Griesmann, U., Brault, J. W., & Abrams, M. C. 2015, Xgremlin: interferograms and spectra from Fourier transform spectrometers analysis, Astrophysics Source Code Library, ascl:1511.004
Peck, E. R., & Reeder, K. 1972, JOSA, 62, 958
Thorne, A. 1996, PhST, 65, 31
Thorne, A. P., Harris, C. J., Wynne-Jones, I., Learner, R. C. M., & Cox, G. 1987, JPhE, 20, 54
Wallerstein, G., Gilroy, K. K., Zethson, T., Johansson, S., & Hamann, F. 2001, PASP, 113, 1210
Whaling, W., Anderson, W. H. C., Carle, M. T., Brault, J. W., & Zarem, H. A. 1995, JQSRT, 53, 1